ADVANCED FUNCTIONAL MATERIALS
www.afm-journal.de

Boosting Ionic Conductivity and Air Stability in Bromide-Rich Thioarsenate Argyrodite Solid Electrolytes

Ruihua Zhou, Ajay Gautam, Emmanuelle Suard, Shenghao Li, Swapna Ganapathy, Kai Chen, Xin Zhang, Ce-Wen Nan, Shuo Wang,* and Marnix Wagemaker**

Lithium argyrodite thiophosphate superionic conductors are being explored as promising solid electrolytes for all-solid-state batteries, primarily due to their high ionic conductivity and ease of processing. Yet, these electrolytes present challenges such as chemical instability in humid conditions and incompatibility with cathode materials. Although some lithium argyrodites show improved air stability, their ionic conductivity deteriorates below the practically required value. Herein, based on hard soft acid base theory, a new family of lithium argyrodite, as solid solution $Li_{6-x}AsS_{5-x}Br_{1+x}$ (for $0.0 \leq x \leq 0.6$), has been proposed to address these issues. Through a combination of neutron diffraction, NMR spectroscopy, and electrochemical impedance spectroscopy, it has been determined that the partial substitution of S^{2-} by Br^{-} weakens interactions within the Li^{+} "cage", facilitating long lithium-ion movement throughout the structure. An additional T4 Li^{+} site is identified, offering a lower energy barrier for inter-cage jumps. Consequently, the $Li_{5.5}AsS_{4.5}Br_{1.5}$ member of the composition series exhibits a higher Li-ion diffusivity resulting in a remarkable ionic conductivity of 15.4 mS cm^{-1}. Compared with lithium thiophosphates, the $Li_{5.5}AsS_{4.5}Br_{1.5}$ also shows excellent air stability. This research opens a new avenue for developing air-stable sulfide solid electrolytes with high ionic conductivity necessitated for practical application in solid-state batteries.

1. Introduction

Lithium-ion batteries (LIBs) have revolutionized portable electronics and electric vehicles, where intensive materials and engineering developments have led to their high electrochemical performance and long cycle life.[1,2] However, the use of liquid electrolytes in LIBs presents inherent challenges, including safety risks associated with flammability, leakage, and the potential for dendrite formation with lithium metal anode, which can lead to short circuits and reduced battery longevity.[3–5] To address these limitations, solid-state batteries (SSBs) employing solid electrolytes have emerged as a promising alternative. Solid electrolytes not only mitigate the safety concerns associated with their liquid counterparts but also offer the potential for higher energy densities when paired with lithium/silicon anodes and allow broader operational temperature ranges.[6] A variety of solid electrolytes have been explored, including oxides, phosphates, lithium halides, and lithium argyrodites ($Li_{6-x}PS_{5-x}X_{1+x}$, X = Cl and Br).[7–12] Notably, lithium argyrodites have garnered considerable attention due to their superior ionic conductivity, advantageous mechanical properties, and straightforward synthesis.[12] Progressing these advantages into applicable materials, achieving higher ionic conductivity and good air stability in solid electrolytes becomes paramount, as it directly influences the faster charge/discharge rates production costs, and longer cycle life of SSBs.

R. Zhou, S. Li, X. Zhang, S. Wang
Center of Smart Materials and Devices
State Key Laboratory of Advanced Technology for Materials Synthesis and Processing
School of Material Science and Engineering
Wuhan University of Technology
Wuhan 430070, China
E-mail: shuowang@whut.edu.cn

A. Gautam, S. Ganapathy, M. Wagemaker
Storage of Electrochemical Energy
Department of Radiation Science and Technology
Faculty of Applied Sciences
Delft University of Technology
Mekelweg 15, Delft 2929JB, The Netherlands
E-mail: A.AjayGautam@tudelft.nl; m.wagemaker@tudelft.nl

The ORCID identification number(s) for the author(s) of this article can be found under https://doi.org/10.1002/adfm.202420971

E. Suard
Institut Laue-Langevin
Grenoble 38042, France

K. Chen
QingTao (Kunshan) Energy Development Co., Ltd.
Suzhou 215334, China

C.-W. Nan
State Key Laboratory of New Ceramics and Fine Processing
School of Materials Science and Engineering
Tsinghua University
Beijing 100084, China

DOI: 10.1002/adfm.202420971

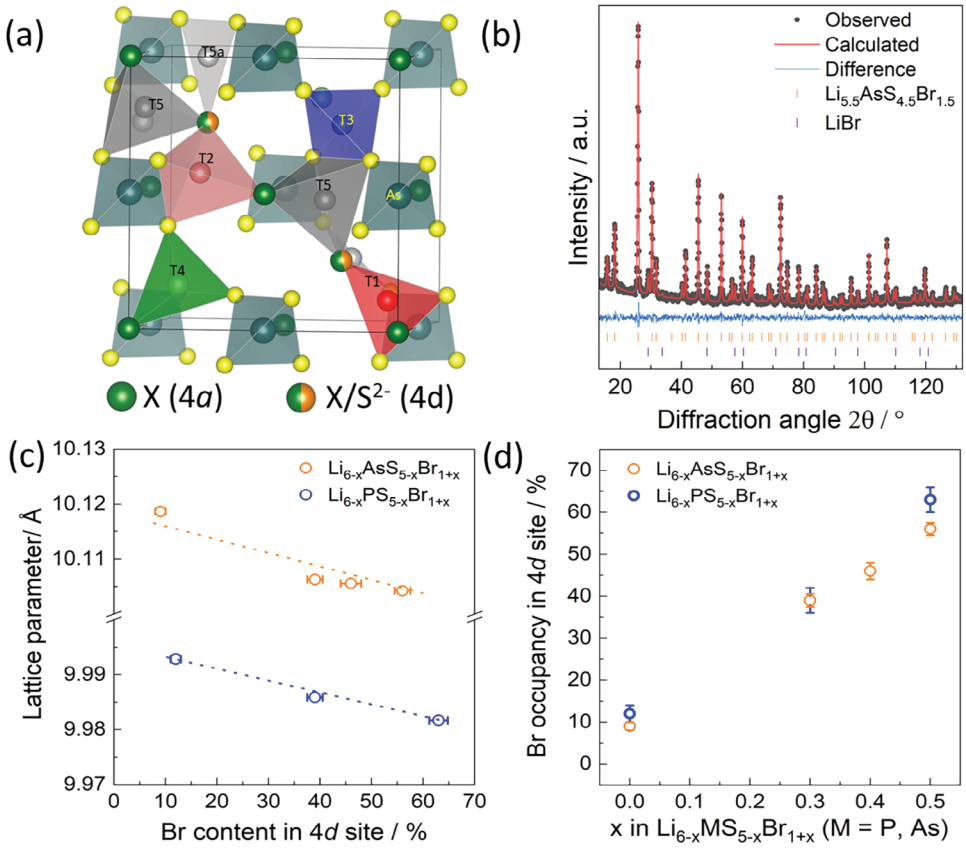

Figure 1. a) $Li_{6-x}AsS_{5-x}X_{1+x}$ argyrodite framework showing Wyckoff positions: X^- and S^{2-} at the 4d site, with X^- occupying the 4a site. The lithium argyrodite framework has 136 interstitial voids, 4 voids are occupied by $(As/P)^{5+}$, forming $(As/P)S_4^{3-}$ units. The remaining voids can be occupied by lithium with different configurations: T1 (red), T2 (pink), T3 (blue), T4 (green), and T5 (gray). b) Analysis of neutron diffraction data via Rietveld refinement of $Li_{5.5}AsS_{4.5}Br_{1.5}$. c) Lattice parameter with Br occupancy at the Wyckoff 4d position. d) Bromide occupancy in Wyckoff 4d position as a function of total bromide content. The uncertainty in Figure 1c,d has been calculated using TOPAS software. The uncertainty in lattice parameters is smaller than the size of the circles.

A deeper insight into the composition and optimization conduction mechanism is essential for further enhancing Li-ion conductivity. Several approaches have been investigated to enhance the conductivity of argyrodites including the incorporation of halogen atoms, iso-substitutions, and aliovalent substitutions etc.[7,8,13–16] Lithium argyrodite crystalline materials (Li_6PS_5X, X = Cl, Br, and I) are mostly found with a cubic symmetry and a space group of $F\bar{4}3m$, as initially presented by Deiseroth and colleagues.[17–21] In this face-centered cubic arrangement, the halogen ions are positioned at the Wyckoff 4*a* sites, and free S^{2-} ions, not linked to P, fill half of the tetrahedral Wyckoff 4*d*. P^{5+} (forming the PS_4^{3-} tetrahedra) occupied the octahedral void.[22,23] The remaining voids are available for lithium occupation, are categorized as lithium tetrahedra $Li(S/X)_4$ (which share -face, edge, corner) with PS_4^{3-} and are termed as T1-T5a as shown in **Figures** 1a and S1a,b (Supporting Information). The T5, T2, T4, and T5a collectively form the cage-like framework around the free S^{2-} 4*d* site, as visualized in Figure S1c (Supporting Information), which paves the way for the 3D Li^+ network within the structure.[9]

Early studies predicted the lithium diffusion pathway in argyrodite: jumps within the cage (both intra-cage and doublet) and jumps between cages (inter-cage).[24,25] Masuda et.al have investigated the substructure of lithium argyrodites in $Li_{7-x-y}(PS_4)(S_{2-x-y}Cl_xBr_y)$, uncovering occupancy of T4 lithium positions, proposing specific inter-cage diffusion pathways.[26] Density functional theory (DFT) analysis shows that Si^{4+} substitution in $Li_{6+x}P_{1-x}Si_xS_5Br$ increases T4 Li occupancy and redistributes lithium ions, consequently enhancing lithium mobility across lithium cages.[27] In the different sulfide argyrodite compositions, different lithium site occupancies have been observed (T2, T3, or T4).[23,27] For example, the Sn-enriched thioantimonate argyrodites identified T2 and T3 site occupancies,[28] while Br-enriched $Li_{5.5}PS_{4.5}Br_{1.5}$ revealed T4 site occupancies.[23] Overall, both (first is via adjacent T2 sites and the second via T5 sites through the T4 site as shown in Figure S1a,b, Supporting Information) inter-cage jumps indicated in Figure S1a,b (Supporting Information) are considered as the rate-limiting step due to their high energy barrier.[23]

Anion site disorder, the partial halogen occupancy on the "free" sulfur *4d* site, was early on recognized to have a large impact on the long range Li-ion diffusivity.[24] For instance, iodide argyrodite has an ordered structure where the 4*a* site is exclusively occupied by I^- and the 4*d* site by S^{2-} due to the large

mismatch in ionic radii, resulting in only localized Li-ion mobility. In contrast, chloride and bromide argyrodites exhibit higher site disorder, where Cl^-/Br^- (chloride/bromide ions) occupy ≈60% and 20% of the 4*d* site, respectively, and display a three orders of magnitude higher ionic conductivity. DFT simulations suggested that an optimal conductivity is achieved with ≈75% site disorder, where the rates of the three ion jump types—doublet, intra, and inter-cage—are balanced.[24] In line with this, the incorporation of higher halide content has been shown to enhance ionic conductivities in lithium argyrodite significantly. For example, Adeli et al.[29] demonstrated that chloride substitution in $Li_{6-x}PS_{5-x}Cl_{1+x}$, ($x \leq 0.5$) with 82% chloride at the 4*d* site, resulted in a notable increase in conductivity to 9 mS cm^{-1} at x = 0.5. Similarly, Li et al.[24] reported an improved ionic conductivity of 9.6 mS cm^{-1} for a bromide/chloride-enriched composition of $Li_{5.5}PS_{4.5}Cl_{0.8}Br_{0.7}$, where Cl/Br occupied 70% at 4*d* site, thereby underlining the potential of halide enrichment clear interest in solid electrolytes.

Although many lithium thiophosphate argyrodites show high ionic conductivity when compared with oxide SEs,[30] they show poor air stability and release of harmful H_2S gas when exposed to moisture.[31,32] Recent studies indicate that replacing a portion of the hard acid P^{5+} with softer acids like Ge^{4+}[33] Sn^{4+}[34] As^{5+}[35] Sb^{5+}[36] could enhance the air stability of P-based sulfide SEs, using Hard Soft Acid Base (HSAB) theory.[37,38] When considering sulfide SEs with only soft acids as central cations, their moisture stability sequence is $As^{5+} > Sn^{4+} > Ge^{4+} > Sb^{5+}$, according to theoretical thermodynamic analysis. Some P-free thio-LISICON ($Li_{4-x}Ge_{1-x}As_xS_4$,[39] $Li_{4-x}Sn_{1-x}As_xS_4$,[35] and $Li_{4-x}Sn_{1-x}Sb_xS_4$[36]) have been developed, showing improved moisture resistance and even the ability to recover their ionic conductivity after post-thermal treatment.[35] However, their ionic conductivities at room temperature are typically below 2 mS cm^{-1} which hinders practical application in solid-state batteries. Recently Lu et al. reported the family of P-free argyrodites $Li_{6+x}M_xAs_{1-x}S_5I$ (M = Si, Sn)[37] which exhibit higher conductivity of ≈10 mS cm^{-1} at room temperature and improved air stability. One parameter, that yet remains unexplored is the impact of bromide substitution on the air stability of P-free argyrodites ($Li_{6-x}AsS_{5-x}Br_{1+x}$). It is important to gain a deeper understanding of the structure-conductivity relationships, especially for identifying moisture-resistant compositions.

In this study, we introduce a novel series of thioarsenate bromide-rich argyrodites $Li_{6-x}AsS_{5-x}Br_{1+x}$ ($0.0 \leq x \leq 0.6$), making use of Hard Soft Acid Base (HSAB) theory, resulting in materials that exhibit excellent air stability. In addition tuning the bromide content on the 4*a* and 4*d* site, a very high ionic conductivity is achieved. The $Li_{6-x}AsS_{5-x}Br_{1+x}$ series are synthesized via facile solid-state reaction. Through comprehensive characterization, including neutron diffraction, NMR spectroscopy, and electrochemical impedance spectroscopy, we elucidate the impact of halide/arsenic substitution on both the lithium substructure and its related to transport mechanisms within the $Li_{6-x}AsS_{5-x}Br_{1+x}$ framework. Notably, compared with lithium thiophosphate, the unit cell and lithium site volumes are larger in thioarsenates series, which is considered favorable for ionic conductivity. With the increasing substitution of S^{2-} by Br^- in $Li_{6-x}AsS_{5-x}Br_{1+x}$ series, the connectivity of lithium cages is enhanced, and T4 Li occupancy by is observed, which providing in a lower energy barrier for the rate-limiting step, thereby improving Li-ion transport. Finally, the excellent air stability of the $Li_{6-x}AsS_{5-x}Br_{1+x}$ is demonstrated by air exposure tests.

2. Results and Discussion

2.1. Structure of $Li_{6-x}(As/P)S_{5-x}Br_{1+x}$

Lithium argyrodite, Li_6PS_5X, (X = Cl, Br, or I) demonstrates structural disorder, specifically between the X^- and S^{2-} ions at the 4*d* sites, which has been correlated to the Li-ion conductivity. Recent findings highlight that the degree of structural disorder within Li_6PS_5Br can be modulated through the synthesis method or by increasing Br content.[23] Additional substitution of S^{2-} with Br^- has proven to raise the structural disorder and enhance ionic conductivity significantly. However, how this in combination with replacing phosphorus (P) with arsenic (As), aiming for improved air stability in combination with high conductivity, affects the lithium substructure, structural framework, and ionic transport mechanisms are yet to be fully understood. To comprehend the impact of such cation substitution and increased bromide content on the structure and ionic transport of lithium argyrodites, we synthesized a series of lithium thioarsenate and thiophosphate argyrodites ($Li_{6-x}AsS_{5-x}Br_{1+x}$, $x \leq 0.6$ and $Li_{6-x}PS_{5-x}Br_{1+x}$, $x \leq 0.6$) using solid-state reactions. We conducted neutron diffraction measurements and analyzed the data using Rietveld refinement to gain deeper insight into structural changes and Li^+ substructures and how this affects Li-ion conductivity. The $Li_{6-x}AsS_{5-x}Br_{1+x}$ series exhibited a cubic structure across all compositions, assigned to the $F\bar{4}3m$ space group, as detailed in Figures S2–S5 (Supporting Information).

In the thiophosphate $Li_{6-x}PS_{5-x}Br_{1+x}$ series, the solubility limit was found at x = 0.5, indicating that free S^{2-} is not entirely substitutable by the bromide anion.[23,40] For the thioarsenate $Li_{6-x}AsS_{5-x}Br_{1+x}$ series, we observe the pronounced emergence of LiBr (8 wt.%) and Li_3AsS_4 (2.2 wt.%) side-phases at compositions of x = 0.6 as seen in the neutron diffraction data (Figure S5, Supporting Information). This suggests the solubility limit for this series lies between 0.5 and 0.6. Figure 1b shows a Rietveld refinement of one composition of this series, i.e., $Li_{5.5}AsS_{4.5}Br_{1.5}$ (all refinements and structural information can be found in Figures S2–S5, Supporting Information). The samples contained minor impurity phases of LiBr (up to 3.0 wt.%), but these impurities were unlikely to impact ionic transport or structural analysis. The SE particle morphology and elemental distribution were measured via SEM with EDX (Figure S6, Supporting Information). The average particle size of the $Li_{5.5}AsS_{4.5}Br_{1.5}$, Li_6AsS_5Br, $Li_{5.5}PS_{4.5}Br_{1.5}$, and Li_6PS_5Br is ≈5 µm each. The EDX results show that each element is uniformly distributed on the micrometer level, indicating no obvious impurities exist.

Diffraction analysis revealed that the thioarsenate series exhibits larger unit cells than the thiophosphate series, as illustrated in Figure 1c and Figure S7 (Supporting Information). This expansion, ≈0.12 Å, is attributed to the larger ionic radius of As^{5+} compared to P^{5+}. With an increase in Br content in the thioarsenate series, the lattice parameters correspondingly decrease, although the Br occupancy at the 4*a* site remains relatively unchanged which is associated with the unit cell parameter (Figure S8, Supporting Information). This observation aligns with

previous findings ($Li_{6-x}PS_{5-x}Cl_{1+x}$ and $Li_{6-x}PS_{5-x}Br_{1+x}$ series[23,29]) and indicates that increased Br content induces Li^+ vacancies and changes in the Li^+ substructure, thus reducing lattice parameters. Figure 1d displays the percentage of Br at the Wyckoff 4*d* site as a function of total Br content. As the Br content (x) increases, Br is distributed across the 4*d* sites within the argyrodite structure, starting from 9% at x = 0.0 and reaching 56% at x = 0.5. For thiophosphate series, the starting of the Br occupancy on the 4*d* site is from 10% at x = 0.0, increasing to 63% at x = 0.5. The trend observed in both series of materials is consistent; the only difference lies in the absolute values of the lattice parameters, which are higher in the arsenic series compared to the phosphorus series due to the previously mentioned differences in ionic radii.

2.2. The Lithium Substructure

To gain a deeper understanding of the lithium substructure in the $Li_{6-x}AsS_{5-x}Br_{1+x}$ series, we employed neutron powder diffraction that was analyzed with Rietveld refinement. We used the Li_6PS_5Br material (ref. [23]) as an initial model for refining both lithium positions and occupancies. **Figure 2a** displays the lithium occupancy across the thioarsenate argyrodite series as a function of bromide content. From Rietveld refinement has identified five distinct lithium sites: T5, T2, T5a, T3, and T4, each occupied to varying degrees depending on the compositions. The overall Li^+ content was constrained to according to charge balance with the refined Br content.

Recent studies investigating the lithium substructure of $(Li_{7-x-y}(PS_4)(S_{2-x-y}Cl_xBr_y)$, and $Li_{6-x}PS_{5-x}Br_{1+x}$ found two inter-cage pathways (the first via adjacent T2 sites and the second via T5 sites through the T4 site as shown in Figure 2b,c) that appear crucial for long-range Li^+ diffusion.[23,26] Additionally, bond valence sum calculations suggest that the inter-cage jump via the T4 site has lower energy barriers for these compositions.[7,26] In the present thioarsenate series, we determined the T4 and T2 occupancies and the jump distances, T2−T2 and T5−T4−T5, as functions of bromide content, shown in Figure 2e,f. As the bromide content increases, the T2−T2 and T5−T4−T5 distances decrease. The T5−T4−T5 distance decreases from 3.80 (5) Å at x = 0.0 to 3.70 (5) Å at x = 0.5. The T2−T2 distance decreases from 2.46(6) at x = 0.0 to 1.80(5) Å at x = 0.5. This suggests that an increase in bromide content results in shorter inter-cage distances and therefore more diffusion between the cages. Figure S9 (Supporting Information) reveals that the volumes of T5, T2, and T4 polyhedral are only slightly affected by variations in bromide content. Figure 2d and Figure S10 (Supporting Information) display the transition area of Li-(S_2X) and the volume of $(P/As)S_4^{3-}$ tetrahedra as a function of bromide content. With the replacement of phosphorus by arsenic, the tetrahedral volume of $(P/As)S_4^{3-}$ expands from 4.41 to 5.2 Å^3, and the transition area of Li-(S_2X) increases from 2.29 to 2.34 Å^2, all of which broaden the lithium-ion diffusion pathways. The charge distribution on the Wyckoff 4*d* and Wyckoff 4*a* sites influences the surrounding Li^+ substructure. To explore how bromide affects Li^+ arrangement, we extended the calculation of the average Li^+ distribution, as expressed as the mean radius of the Li cage, R_{mean}, to include all sites determined by Rietveld refinement. R_{mean} is calculated by averaging the distances from the central 4*d* anion (usually S^{2-}) to various Li^+ sites (T2, T5, T5a, T3, and T4), and then dividing this by the number of Li^+ ions at specific sites within a single cage. A graphical depiction of R_{mean} is presented in Figure 2g. As we increased the bromide content in the thioarsenate argyrodite, we observed a concomitant increase in the R_{mean} values (see Figure 2h). A larger R_{mean} value signifies an expansion of the Li^+ cage, which in turn shortens the T5−T4 distances, enhancing the connectivity between cages and thereby enhancing long range ionic diffusion. This observation is also corroborated by changes in chemical shift observed upon bromine addition from the room-temperature ^{6}Li MAS NMR spectra (Figure 2i). For Li_6AsS_5Br the ^{6}Li resonance is observed at 2.53 ppm. As the bromide content increases, the ^{6}Li resonance shifts upfield to lower ppm values (Figure 2i) indicating that the Li-ions are more shielded. This can be explained by the positive charge lithium ion strongly attracted to S ion than Br ion at the 4*d* site in the center of the cage. This leads to an increase in R_{mean} and contributes to the shift of the ^{6}Li peak to lower ppm values.

2.3. Ionic Transport

To examine the influence of Br content on the ionic conductivity of the $Li_{6-x}AsS_{5-x}Br_{1+x}$ series, we carried out temperature-dependent impedance spectroscopy to measure the ionic conductivity and determine the activation energy. The temperature varied from −50 to −10 °C in increments of 10 °C, and 25 °C. The impedance data (−50 to −10 °C) were modeled using an equivalent circuit consisting of a resistor and a constant phase element (CPE) in parallel, followed by another CPE in series, representing blocking the behavior of the steel electrode. At higher temperatures, the contribution from the resistor/CPE configuration shifted to higher frequencies beyond the measurable range of the experiment, allowing only the tail of the electrode-blocking behavior to be considered in the impedance fitting. **Figure 3a** displays the Nyquist plots of the $Li_{6-x}AsS_{5-x}Br_{1+x}$ series at −50 °C, with additional temperature data available in the supplementary material (Figure S11, Supporting Information). From the impedance data, the room temperature ionic conductivities of $Li_{6-x}AsS_{5-x}Br_{1+x}$ series are determined. With increasing the Br content, the ionic conductivity shows a dramatic increase from 2 to 15.4 mS cm^{-1}, which to the best of our knowledge is the highest ionic conductivity obtained in the lithium argyrodites series prepared by cold pressing. This enhancement in ionic conductivity correlates closely with changes in the lattice parameters. The substitution of divalent sulfide S^{2-} with monovalent bromide Br^- and the introduction of Li^+ vacancies lead to lattice shrinkage. This lattice shrinkage, combined with the expansion of Li-cages and the reduction in inter-cage jump distances, significantly influences ionic conductivity, as illustrated in Figure S12 (Supporting Information).

The replacement of S^{2-} by Br^- reduces the average anionic charge density at the Wyckoff 4d site. Lithium ions form cage-like structures around these sites, and the substitution weakens the bonding environment between Li and the Wyckoff 4d centers. This results in an expansion of the lithium cages and a decrease in inter-cage distances, as shown in Figure 2e. These structural changes—lattice shrinkage, expanded Li-cages, and reduced

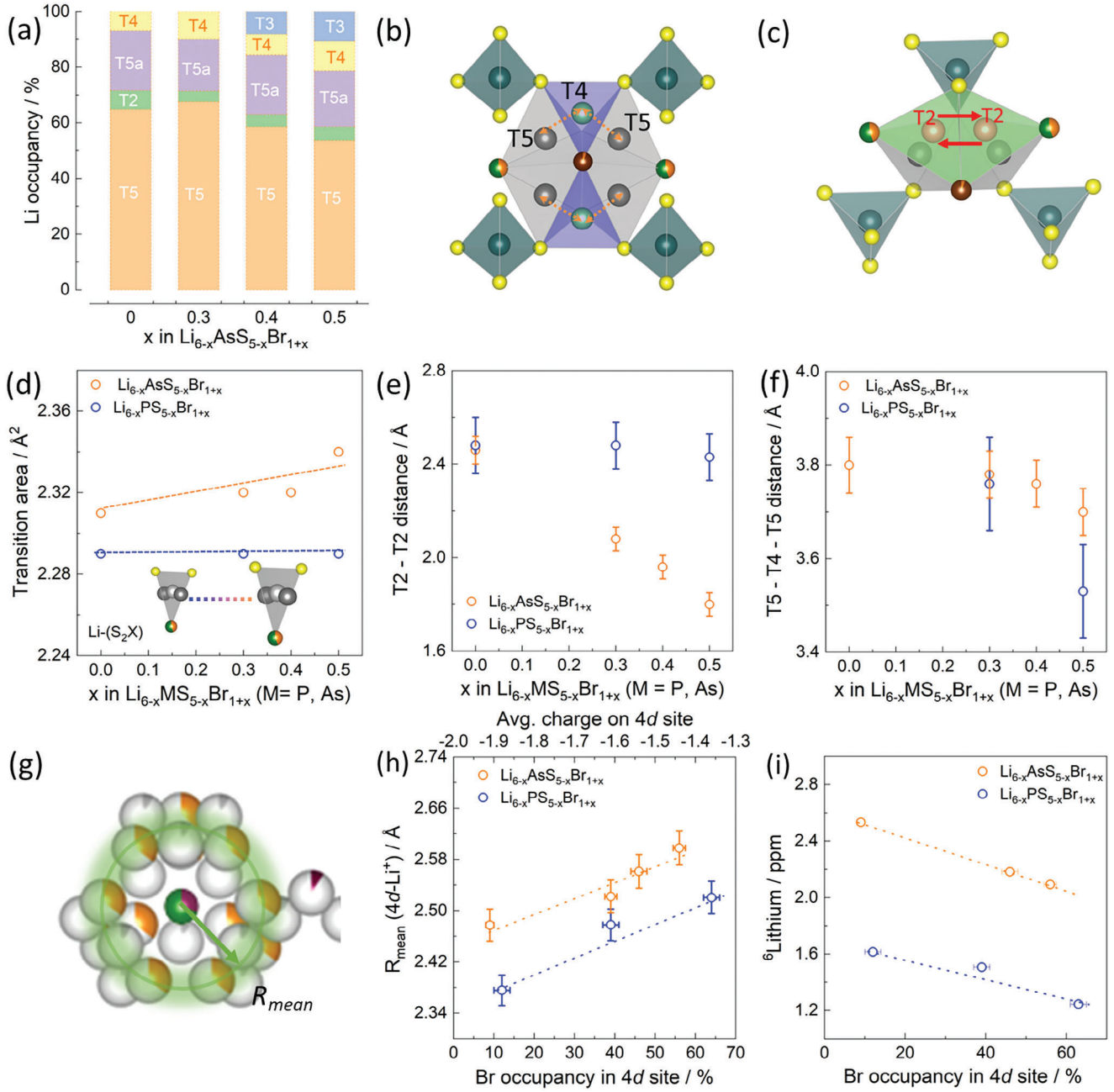

Figure 2. a) The Li^+ distribution across the different sites of $Li_{6-x}AsS_{5-x}Br_{1+x}$ as a function of Br content. b) A lithium jump pathway connecting two T5 sites via a T4 site (T5–T4–T5). c) Second lithium jump pathway through two neighboring T2 sites (T2–T2). d) The transition area of Li-(S_2X) as a function of bromide content. The inter-cage lithium-ion pathway distances: e) between T2–T2 and f) the linked pathway from T5 through T4 to T5 as a function of bromide content. g) The visual representation of R_{mean}. h) the average Li^+ distribution, R_{mean}, representing the radius of the sphere formed by Li positions centered around the anion position (Wyckoff 4d, S^{2-}). As the Br content increases or the Br occupancy on 4d site increases, the average charge on the 4d site decreases as the divalent S is replaced by monovalent Br. This causes R_{mean} to increase, representing an expansion of lithium cage and decrease the inter-cage jump distance.i) ^6Li chemical shift value of $Li_{6-x}AsS_{5-x}Br_{1+x}$ as a function of the Br content, the chemical shift decreases with increasing Br content, further indicating a change in the local Li^+ environment. The uncertainty in Figure 2d–i has been calculated using TOPAS software. The uncertainty in transition area is smaller than the size of the circles.

inter-cage distances—work together to enhance ionic conductivity. The non-linear relationship between Br occupancy at the Wyckoff 4d site and ionic conductivity is depicted in Figure S13 (Supporting Information), emphasizing the critical role of Br in facilitating lithium transport. Additionally, Figure 3b illustrates the diffusion coefficient obtained from with pulsed field gradient (PFG) NMR measurements, demonstrating an increase from 2.25×10^{-12} to 1.6×10^{-11} m^2 s^{-1} with the increase of bromide content. This suggests that the higher lithium diffusion coefficient is responsible for the enhancement in ionic conductivity by

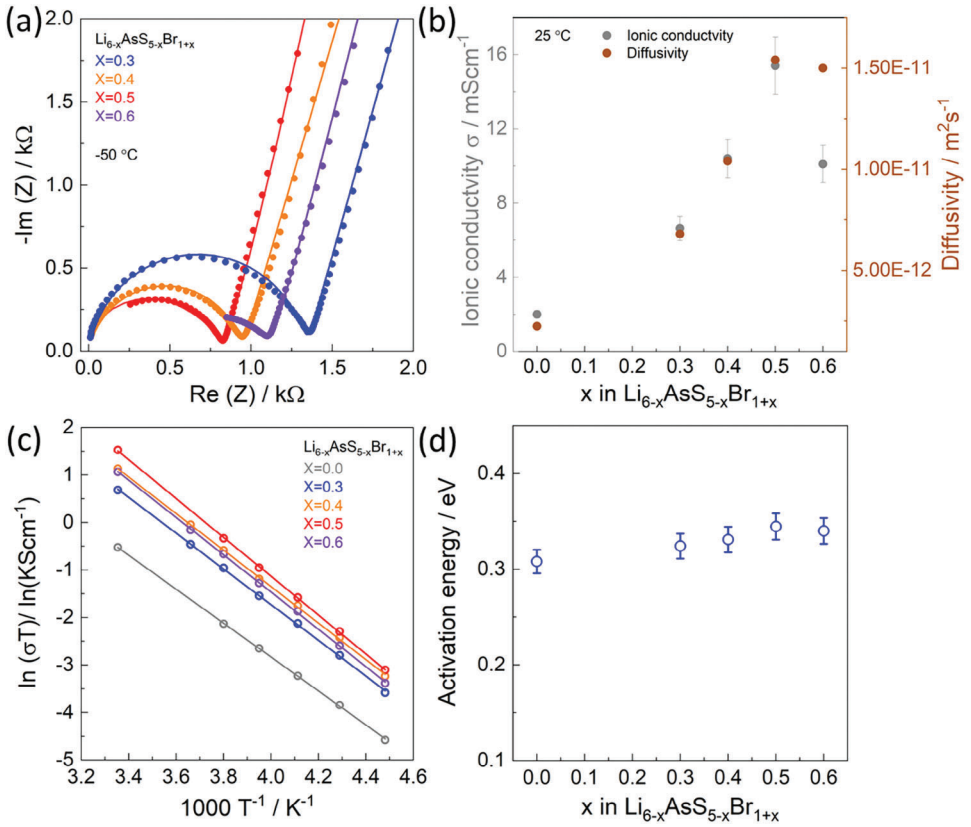

Figure 3. a) Representation of impedance response of the $Li_{6-x}AsS_{5-x}Br_{1+x}$ series at a temperature of −50 °C. The closed circles indicate the impedance response of the electrolyte and exhibited α value of 0.89–0.92, corresponding to bulk transport. b) Ionic conductivities and diffusion coefficient at room temperature and measured by impedance spectroscopy and pulsed field gradient NMR respectively, c) Represents Arrhenius plots, obtained from temperature-dependent impedance spectroscopy. and d) activation energy (E_A) of $Li_{6-x}AsS_{5-x}Br_{1+x}$ as a function of the Br content. The uncertainties in Figure 3b,d correspond to 3σ.

a factor of 7 in $Li_{5.5}AsS_{4.5}Br_{1.5}$, compared to Li_6AsS_5Br. However, a notable difference in ionic conductivity (from EIS) and diffusion coefficient (from PFG NMR measurements) was observed for the composition x = 0.6. The diffusion length, calculated using the equation: $x = \sqrt{6Dt}$ was ≈0.346 µm for a diffusion coefficient of 1.5×10^{-11} m^2 s^{-1} and a diffusion time of 20 ms. Given that the particle size, determined via scanning electron microscopy, is ≈5 µm, the diffusion length is consistent with the particle size. Additionally, we observed higher impurities in the x = 0.6 compositions of LiBr (8 wt.%) and Li_3AsS_4 (2.2 wt.%) side-phases. Impedance measurements on samples with thicknesses ranging between 1200 and 1300 µm were used to determine ionic conductivity. These findings suggest that the higher diffusion coefficient observed is due to diffusion within the solid electrolyte particle size, while the differences in ionic conductivity are influenced by the presence of impurity phases at x = 0.6. Figure 3c reveals that the temperature-dependent ionic conductivities follow a linear Arrhenius trend, allowing for the calculation of activation energy. Interestingly, Figure 3d shows that the activation energy slightly rises with increased Br content for the thiophosphate (ref. [23]) and thioarsenate argyrodites. Although this may initially appear counterintuitive with improved conductivity, it aligns with the Meyer-Neldel rule or compensation rule (Figure S14a,b, Supporting Information), which has been suggested to be explained as that a higher activation barrier requires more excitations to be crossed by a diffusive element, which raises the entropy of migration term in the Arrhenius pre-factor.[41] The electronic conductivity of the $Li_{5.5}AsS_{4.5}Br_{1.5}$ was determined to be $(1.9 \pm 0.7) \times 10^{-13}$ S cm^{-1} (Figure S15).

While ionic conductivity determined from impedance spectroscopy may account for various charge carriers, grain size, and grain boundary contributions, solid-state ^{7}Li NMR relaxometry specifically probes ion dynamics at the shorter time scale of Li-ion diffusion being sensitive to doublet, intracage, and intercage jumps. **Figure** 4a shows the temperature-dependent ^{7}Li spin-lattice relaxation (SLR) rates ($1/T_1$) for the $Li_{6-x}AsS_{5-x}Br_{1+x}$ series. The temperature dependence of the ^{7}Li SLR rates in the laboratory frame can be used to probe lithium ion dynamics on the timescale of the Larmor frequency (ω_o) which is of the order of 10^{-9} s. This is based on the assumption that the variation in spin–lattice relaxation is primarily induced by Li-ion mobility (hopping) in the Li-containing material. When the hopping frequency aligns with the Larmor frequency (ω_o), the value of relaxation rate $1/T_1$ peak reaches a maximum as a function of

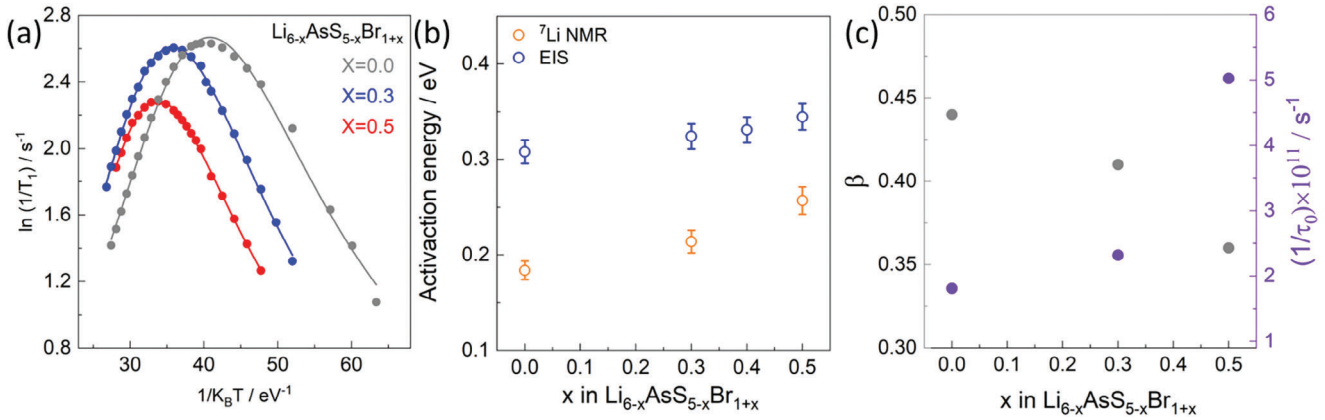

Figure 4. a) Spin-lattice relaxation rates $1/T_1$ measured using a saturation recovery sequence and the fit (lines) using the modified BPP-model for Li_6AsS_5Br, $Li_{5.7}AsS_{4.7}Br_{1.3}$, and $Li_{5.5}AsS_{4.5}Br_{1.5}$. b) The activation energy obtained from the modified BPP model fit and electrochemical impedance spectroscopy. c) The asymmetry parameter β and pre-factor as a function of Br content were obtained from the fit of the modified BPP model. The uncertainties in Figure 4b correspond to 3σ. The uncertainty in Figure 4c is smaller than the size of the circles.

temperature. At the peak maximum, the correlation time τ_c can be estimated as $\omega_o\tau_c \approx 1$. Typically τ_c is very similar to the average residence time τ. This correlation time follows an Arrhenius behavior. In case of 3D uncorrelated motion, the relaxation curve is symmetric and can be fit with the BPP (Bloembergen, Purcell, and Pound) spectral density function. The argyrodites, however, typically manifest an asymmetric relaxation rate curve, better fit with the modified BPP spectral density $(\omega_o) \propto \frac{\tau}{1+(\omega\tau)^{1+\beta}}$. β quantifies this asymmetry and is given by $\beta = \frac{E_a^{LT}}{E_a}$, where E_a is the activation energy determined from the BPP fit and E_a^{LT} corresponds to the activation energy of the low-temperature flank. A symmetric relaxation rate curve has a $\beta = 1$. However, the β values for the Cl- and Br-containing argyrodites are below 1,[16,42] which has been ascribed to the presence of various kinds of jumps occurring in the lithium argyrodite. The low-temperature flank of the relaxation curve have been assigned to more local movement of Li-ions, i.e., doublet and intracage jumps, whereas the high-temperature flank to the more long-range intercage movement. Hereby, a decrease in the β value is indicative of an increase in the total number of intercage jumps.[16,42] Following this assignment, we observe that on increasing the Br content in the present materials, shown in Figure 4b, the β value decreases, indicating that more intercage jumps occur with higher Br contents. From the fits of the relaxation rate curves with the modified-BPP model, we obtain activation energies of 0.121, 0.148, and 0.178 eV for Li_6AsS_5Br, $Li_{5.7}AsS_{4.7}Br_{1.3}$, and $Li_{5.5}AsS_{4.5}Br_{1.5}$, respectively (see **Table 1**). This increase in activation energy and higher β value with Br-content can be attributed to the increase in the amount of intercage jumps, which have a higher activation energy. This is possibly why the relaxation curves shift to higher temperatures of 292, 328, and 349 K for the Li_6AsS_5Br, $Li_{5.7}AsS_{4.7}Br_{1.3}$, and $Li_{5.5}AsS_{4.5}Br_{1.5}$ respectively as seen in Figure 4a. This trend aligns with that observed for the electrochemical impedance data of lithium argyrodite compositions shown in Figure 3d.

Table 1. ^{7}Li Activation energy (E_a), Pre-exponential factor, and asymmetry parameter β as a function of bromide contents.

Sample	Activation Energy [eV]	Pre-Exponential Factor [s^{-1}]	Asymmetry Parameter β
Li_6AsS_5Br	0.184 (9)	1.81×10^{11}	0.44
$Li_{5.7}AsS_{4.7}Br_{1.3}$	0.214 (11)	2.32×10^{11}	0.41
$Li_{5.5}AsS_{4.5}Br_{1.5}$	0.257 (14)	5.03×10^{11}	0.36

2.4. Air Stability

Currently, one of the main obstacles to the large-scale practical application of lithium thiophosphate electrolytes is their poor air stability. When exposed to moisture, lithium thiophosphate electrolytes tend to release H_2S gas, leading to structural damage and degradation of cell performance, as well as increased manufacturing costs. To assess the air stability of the lithium thiophosphate and thioarsenate, $Li_{6-x}(As/P)S_{5-x}Br_{1+x}$ (x = 0, 0.5) solid electrolyte, exposure experiments in a humid nitrogen environment were conducted, and the rate and total amount of released H_2S gas were monitored. As shown in **Figure 5a**, the Li_6PS_5Br electrolyte exhibits the highest released H_2S amount when exposed to a 40% humidity nitrogen environment for 30 min, with the fastest release rate. As the bromine content increases, the amount of released H_2S decreases, and the release rate slows down. This could be attributed to the reduction of free S^{2-} ions in the argyrodite crystal structure after excessive Br substitutions. By substituting P with As, the release amount of H_2S could be further reduced. Moreover, by increasing amount of Br substitution in the Li_6AsS_5Br, the release rate of H_2S gas could be further reduced. Notably, the $Li_{5.5}AsS_{4.5}Br_{1.5}$ electrolyte exhibits the lowest total released amount of H_2S, which is only a quarter of that released by the Li_6PS_5Br electrolyte.

Since the ionic conductivity of sulfide electrolytes is a crucial asset for practical applications, the $Li_{6-x}(As/P)S_{5-x}Br_{1+x}$ (x = 0, 0.5) electrolytes were exposed to an atmospheric environment with a relative humidity of 20%, and the changes of the ionic conductivity were measured to further evaluate their air stability. As depicted in Figure 5b, during the exposure process, the ionic conductivity initially decreases rapidly and then slows down.

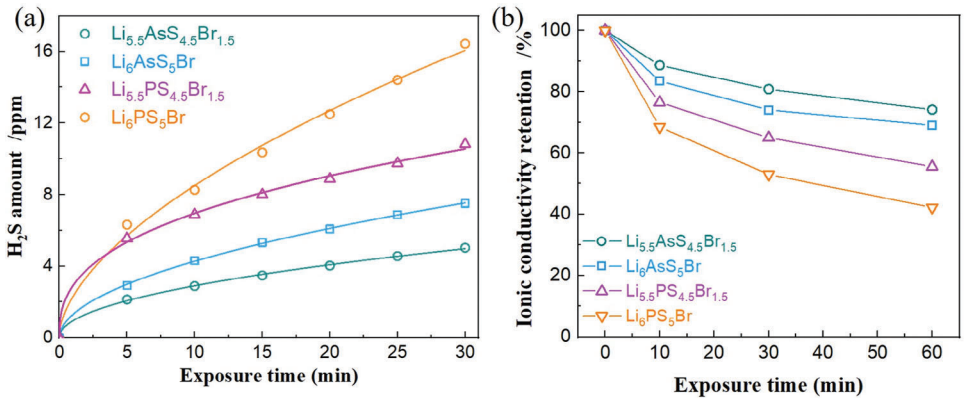

Figure 5. a) The amount of H_2S generated from $Li_{5.5}AsS_{4.5}Br_{1.5}$, Li_6AsS_5Br, $Li_{5.5}PS_{4.5}Br_{1.5}$, and Li_6PS_5Br solid electrolytes as a function of exposure time in 40% nitrogen humidity at room temperature. b) Ionic conductivity retention of the $Li_{6-x}(As/P)S_{5-x}Br_{1+x}$ (X = 0, 0.5) solid electrolytes after different exposure times in the moisture air with humidity of 20% at room temperature.

Notably, the Li_6PS_5Br electrolyte exhibits the fastest decline in ionic conductivity during the first 10 min, indicating a more severe reaction with moisture. After 1 h of exposure, the ionic conductivity retention follows the order: $Li_{5.5}AsS_{4.5}Br_{1.5}$ > Li_6AsS_5Br > $Li_{5.5}PS_{4.5}Br_{1.5}$ > Li_6PS_5Br. Based on the soft and hard acid-base theory, the $Li_{5.5}AsS_{4.5}Br_{1.5}$ prepared by co-substituting As and Br for Li_6PS_5Br exhibits significantly improved air stability. Figure S16 (Supporting Information) shows the XRD patterns of these sulfide electrolytes before and after exposure reveal that all the electrolytes still keep the argyrodite phase, with no significant impurity phases observed. Therefore, the decrease of ionic conductivity after exposure may attribute to the partial decomposition of the sulfides, forming amorphous substances with low ionic conductivity on their surface, which hinders the ionic conduction between sulfide electrolyte particles. To the best of our knowledge, the present $Li_{5.5}AsS_{4.5}Br_{1.5}$ provides the best combination of air stability and high room-temperature ionic conductivity up to date.

When discussing the potential toxicity and environmental impact of arsenic-containing materials such as Li_6AsS_5Br and Li_6AsS_5I ion conductors, it is important to consider both historical context and chemical properties. Arsenic oxides are known for their high toxicity, potentially raising safety concerns about arsenic sulfides as well. However, many naturally occurring arsenic sulfide compounds, such as As_4S_3 in both α and β-dimorphite forms, are also industrially produced on a large scale. Notably, due to their insolubility in water and acids, arsenic sulfides do not dissolve in gastric juices, rendering them non-toxic when ingested.[35,39] Despite these factors, it remains crucial to conduct comprehensive assessments of the toxicity and environmental impact of these materials. Such evaluations should be a priority for future research to ensure the safe and sustainable use of these innovative materials.

2.5. Battery Performance

To verify the applicability of $Li_{5.5}AsS_{4.5}Br_{1.5}$ in ASSBs, the cell with sulfur-MWCNT- $Li_{5.5}AsS_{4.5}Br_{1.5}$ as cathode active material and In/InLi as anode was assembled. Figure S17 (Supporting Information) shows the long-term cycling performance of In/InLi|$Li_{5.5}AsS_{4.5}Br_{1.5}$|sulfur-MWCNT-$Li_{5.5}AsS_{4.5}Br_{1.5}$ cells with an areal loading of 1.53 mg_{sulfur} cm^{-2} at room temperature at 0.2C. The cell delivered an initial high discharge capacity of 1385 mAh g^{-1}. The capacity decreased to 1161.1 mAh g^{-1} at 2nd cycle. After 100 cycles, the cell still delivered a discharge capacity of 885.66 mAh g^{-1} with the Coulombic efficiency of 102%. The above results demonstrate that $Li_{5.5}AsS_{4.5}Br_{1.5}$ is a promising solid electrolyte candidate for all-solid-state lithium-sulfur battery application.

2.6. Structure–Property Relationship

Increasing Br content in the $Li_{6-x}PS_{5-x}Br_{1+x}$ series significantly improves lithium diffusion, resulting in higher ionic conductivity.[23] Substituting phosphorus with arsenic while simultaneously increasing the bromide content prompts us to examine how structural changes, air stability, and lithium dynamics are affected both within and between the lithium cages, leading to the following key observations:

- We successfully achieved full arsenic substitution and a bromide content of x = 0.5 in the $Li_{6-x}AsS_{5-x}Br_{1+x}$ series. By neutron diffraction analysis we observed the structural changes and significant differences in lattice parameters and $(As/P)S_4^{3-}$ volume due to differences in the ionic size of As^{5+} compared to P^{5+}. As bromide content increases, it is distributed across the Wyckoff 4a and 4d sites, inducing changes in the lithium substructure which is critical for Li-ion conductivity.
- Although the bromide content minimally affects the volumes of T2, T5, and T4 polyhedral (as per Figure S9, Supporting Information), it significantly reduces the distance of inter-cage jumps, notably 2 × (T5–T4) and T2–T2 distances. This reduction, along with an increase in the transition area of Li-(S_2Br), potentially facilitates lithium-ion movement between cages, enhancing ionic connectivity.
- With varying bromide content, shifts in R_{mean} were observed (Figure 2h). As bromide replaces sulfide at the 4*d* site, the local

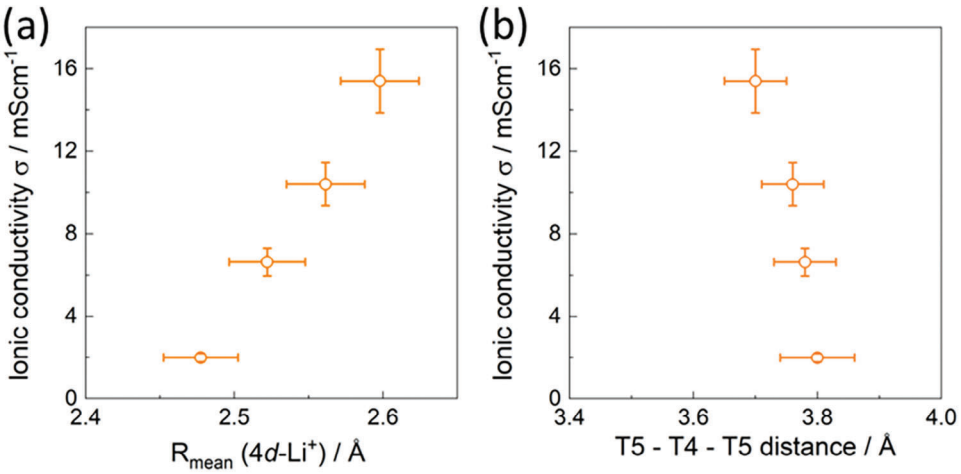

Figure 6. The room-temperature ionic conductivity is shown as a function of a) the R_{mean} distance and b) the T5–T4–T5 distance. An increase in R_{mean} value signifies an expansion of the Li cage away from its center and correlates with increased conductivity and a reduced intercage (T5–T4–T5) distance. The uncertainty in ionic conductivity corresponds to 3σ, and the uncertainty in the T5–T4–T5 distance has been calculated using TOPAS software.

charge decreases, modulating the electrostatic interactions between Li^+-S^{2-} ions. The increase in R_{mean} signifies an expansion of the Li^+ cage and shorter inter-cage distances are critical for enhancing ionic conductivity, as they facilitate the connectivity between the $Li^+ - Li^+$ cages. **Figure** 6a,b illustrates how expanding the lithium cages correlated with improved ionic conductivity, thus supporting more interconnected pathways for enhanced ion transport.

- With increased Br content, ionic conductivity improved from 2 to 15.4 mS cm^{-1}, aligning with findings from spin-lattice relaxation rates $1/T_1$ and PFG NMR that indicate changes in the lithium substructures and enhanced connections through the unit cell, improving lithium-ion diffusion from 2.25×10^{-12} to 1.6×10^{-11} m^2 s^{-1}.
- The primary challenge for large-scale production is the air stability of lithium argyrodite materials. After 1 h of exposure, the ionic conductivity retention follows this order: $Li_{5.5}AsS_{4.5}Br_{1.5}$ > Li_6AsS_5Br > $Li_{5.5}PS_{4.5}Br_{1.5}$ > Li_6PS_5Br. To the best of our knowledge, $Li_{5.5}AsS_{4.5}Br_{1.5}$ currently represents the best-reported lithium argyrodite electrolyte in terms of excellent air stability and high room-temperature ionic conductivity.

3. Conclusion

In conclusion, our study has successfully synthesized bromide-enriched lithium thioarsenate argyrodites, $Li_{6-x}AsS_{5-x}Br_{1+x}$, with varying compositions (x = 0.0 to 0.5), thoroughly investigating the correlation between structure and performance properties through neutron diffraction, solid state NMR and electrochemical impedance spectroscopy. We elucidate the significant impact of bromide/arsenic substitution on the lithium substructure and its correlated transport mechanisms within the $Li_{6-x}AsS_{5-x}Br_{1+x}$ framework. Notably, compared with lithium thiophosphate, lithium thioarsenate exhibits expanded unit cells, increased tetrahedral $(P/As)S_4^{3-}$ volume, and an additional T4 Li^+ site was found which provided a lower energy barrier for the rate-determining jump. As the bromide increased in the thioarsenate argyrodite, we observed an outward expansion of the lithium cage, and a decrease in inter-cage distance (T−T2 and T5−T4−T5 distance), enhancing connectivity between cages and contributing to the higher ionic conductivity, from 2 mS cm^{-1} at x = 0.0 to 15.4 mS cm^{-1} at x = 0.5. Finally, the Br-rich thioarsenate series exhibits excellent air stability via air exposure tests. Our work deepens the understanding of the relationship between lithium sub-structure and ionic transport mechanism of lithium argyrodite solid electrolytes and opens a new avenue for developing novel sulfide solid electrolytes with enhanced ionic conductivity and excellent air stability.

4. Experimental Section

Sample Preparation: The $Li_{6-x}AsS_{5-x}Br_{1+x}$ (for $0.0 \le x \le 0.7$) SEs were prepared by solid-state reaction. The Li_2S (Alfa Aesar, 99.9%), As_2S_3 (Innochem, 99.9%), Sulfur (Aladdin, 99.99%), and LiBr (Acros, 99%) as the starting materials were weighed in an appropriate ratio, and then mixed using a planetary ball mill (FRITSCH PULVERISETTE 7 premium line) at 100 rpm for 2 h. Afterward, the mixture was pressed into pellets and sealed in quartz ampoules using a vacuum sealing machine (VS-Q2, Guangzhou SunJune technology Co. Ltd.). Next, the ampoules were annealed at 450 °C for 6 h with a heating rate of 1.5 °C min^{-1} and then cooled down to room temperature naturally. Finally, the pellets were manually ground to the fine powder and kept in an argon-filled glove box for further structural characterization.

For the $Li_{6-x}PS_{5-x}Br_{1+x}$ series, the precursors Li_2S (Merck, 99.98%), P_2S_5 (Sigma–Aldrich, 99%), and LiBr (Sigma–Aldrich, 99.99%) were weighed in appropriate ratios and then ball-milled at 550 rpm for 25 h. Subsequently, the precursor mixtures were annealed: at 550 °C for compositions with x = 0.0 and at 430 °C for compositions with x = 0.3 and 0.5. The annealing process for 2 h and then allowed the natural cooling. Detailed preparation procedures for this compound series can be found in ref. [23].

X-Ray Diffraction: The phase and purity of the lithium argyrodite materials were determined by using an X-ray diffraction diffractometer (SmartLab SE, Rigaku Corporation) with a Cu K_α radiation source. The 2θ scan range was set between 10° and 90°. To avoid side reactions with moisture and oxygen, samples were sealed in an airtight holder covered with a Kapton polyimide film inside an Argon-filled glovebox.

Scanning Electron Microscopy (SEM): The morphology of the SE particles was obtained by SEM (JSM-7610F) at an acceleration voltage of 15 kV together with energy-dispersive X-Ray spectroscopy.

Air Stability Measurements: One hundred milligrams of the $Li_{5.5}AsS_{4.5}Br_{1.5}$, Li_6AsS_5Br, $Li_{5.5}PS_{4.5}Br_{1.5}$, Li_6PS_5Br electrolyte powders were pressed into a 10 mm pellet with at 150 MPa. The pellet were exposed to moist nitrogen (40% relative humidity) gas for 30 min in a sealed container (40 000 cm^3). The amount of H_2S gas generated was calculated from the H_2S concentration measured with an H_2S gas sensor (RA2000-H_2S, Shenzhen Ruian Electronic Technology Co., Ltd). In addition, XRD and ionic conductivity measurements of all samples were performed before and after exposure to moist air (20% relative humidity) to examine the air stability.

Neutron Powder Diffraction: Neutron powder diffraction measurements were conducted using the D2B high-resolution powder diffractometer at the Institut Laue-Langevin (ILL, Grenoble, France), employing a monochromatic neutron wavelength of $\lambda = 1.5943(10)$ Å. For each sample ≈1.5 g was loaded into a 6-mm-diameter cylindrical vanadium can under an argon atmosphere and then sealed using indium wire to prevent air exposure during transportations. The samples were measured for 4 h each from $10° < 2\theta \leq 160°$ under argon atmosphere.

Electrochemical Impedance Spectroscopy: Electrochemical impedance spectroscopy was conducted using an Autolab PGSTAT combined with an EC10 M impedance analyzer to determine the total ionic conductivity and activation energy. All measurements used a 0.01 V amplitude and a frequency range from 10 MHz to 100 mHz. Around 200 mg of each of the powders were pressed into 10 mm diameter pellets under a pressure of 380 MPa for a duration of 1 min. Stainless steel discs were affixed to both sides for better contact. The temperature range of −50 to 10 °C, incremented by 10 and 25 °C (utilizing a Fryka Climate Chamber) was measured. Impedance spectra analysis was carried out using the RelaxIS 3−Impedance Spectrum Analysis tool.

Electronic Conductivity Measurements: One hundred milligrams of $Li_{5.5}AsS_{4.5}Br_{1.5}$ electrolyte powders were compressed into 10 mm pellets at 150 MPa using a homemade Swagelok cell. Two stainless steel disks were employed as current collectors. Voltages of 0.2, 0.4, 0.6, 0.8, and 1.0 V were applied for 6 h to determine the partial electronic conductivity of solid electrolyte.

Rietveld Refinement: The Rietveld refinements of neutron diffraction data were conducted using TOPAS V7 software,[43] and the initial structural parameters were taken from Li_6PS_5Br study (ref. [23]). The quality of the fit was evaluated using goodness-of-fit (GOF) and R_{wp}. Chebyshev function with 15 coefficients was employed for the background, and a modified pseudo-Voigt function was used for peak shape. The scale factor, zero shift, lattice parameter, isotropic atomic displacement, and atomic occupancies for S^{2-} and Br^- ions at specific Wyckoff positions were refined, ensuring their combined occupancies remained constant. Multiple parameters were refined simultaneously to ensure refinement stability. Lithium positions and occupancies were determined, excluding those with negative thermal displacement as they considered the below the detection limit. The lithium content was fixed for charge balance with the refined Br content. Details on anion/cation occupancy constraints are provided in Tables S2–S5 (Supporting Information).

Solid State NMR: Magic angle spinning (MAS) solid-state ^6Li NMR measurements were conducted using a Bruker Ascend 500 magnet with a static magnetic field B_0 of 11.7 T, paired with a NEO console, yielding a ^6Li Larmor frequency of 73.6 MHz. Sample powders were loaded into 4 mm diameter zirconia rotors, and a MAS speed of 5 kHz was employed. The spin-lattice relaxation time (T_1) was ascertained via a saturation-recovery pulse sequence. Both the 90-degree pulse and T_1 were individually determined for each sample. To ensure complete relaxation, a recycle delay of five times the T_1 was applied for the single pulse spectra. All spectra were calibrated against LiCl in water, set at 0 ppm.

Static solid-state NMR ^7Li relaxation measurements were conducted using a Bruker Ultrashield 300 magnet with a static magnetic field B_0 of 7.1 T with an Avance console yielding a ^7Li Larmor frequency ($\omega/2\pi$) of 116.642 MHz. Chemical shifts were referenced with respect to a 0.1 M LiCl solution. The $Li_{6-x}AsS_{5-x}Br_{1+x}$ series was sealed in PVC tubes within an argon-filled glove box (H_2O, $O_2 < 2$ ppm). Variable temperature T_1 measurements were carried out using a 5 mm static probe. The tests were conducted over a temperature range of -50–+150 °C. Custom Python scripts were employed for the analysis of the NMR data.

All-Solid-State Batteries Assembly: The detailed preparation process of sulfur-MWCNT-$Li_{5.5}AsS_{4.5}Br_{1.5}$ composite cathode was as follows. First of all, the block sulfur was initially ball milled at 600 rpm for 24 h to obtain a submicron sulfur powder. Then, the fine sulfur powders were mixed with Multiwalled carbon nanotubes (MWCNT) in a weight ratio of 60:40 and the ball milled at 300 rpm for 1.5 h to obtain the sulfur-MWCNT composite. After that, the composite was mixed with $Li_{5.5}AsS_{4.5}Br_{1.5}$ in a weight ratio of 40:60 and the ball milled at 300 rpm for 1.5 h to obtain the final composite cathode. First, 80 mg of $Li_{5.5}AsS_{4.5}Br_{1.5}$ powers were pressed into pellet to form the separator under 100 MPa. Then, 5 mg of composite cathode was spread on one separator layer and pressed under 50 MPa. After that, an indium foil and a lithium foil were sequentially attached to the other side of the separator and pressed at 100 MPa. Finally, the battery was pressed at 150 MPa for 3 min. A stack pressure of ≈150 MPa was applied to the cells during cycling. Galvanostatic cycling of the cell was conducted in a potential range of 1.62–3.32 V versus Li^+/Li at 0.2 C at room temperature using a LANHE battery testing system (CT3001A).

Supporting Information

Supporting Information is available from the Wiley Online Library or from the author.

Acknowledgements

This work was supported by the Natural Science Foundation of China (grant no. 52388201 and 52302305) and the Natural Science Foundation Exploration Program of Wuhan (Morning Light Plan) (grant no. 202401jc0089), and support from Tong xiang Advanced New Materials Institute. BatteryNL – Next Generation Batteries based on Understanding Materials Interfaces' project (with project number NWA.1389.20.089) of the NWA research program "Research on Routes by Consortia (ORC)" funded by the Dutch Research Council (NWO). The authors would like to thank HA for fruitful discussions. Neutron powder diffraction experiments were conducted using the D2B high-resolution powder diffractometer at the Institut Laue-Langevin (ILL), Grenoble, France, (Proposal No: EASY-1182, https://doi.ill.fr/10.5291/ILL-DATA.EASY-1182).

Conflict of Interest

Dr. Kai Chen is employed by QingTao (Kunshan) Energy Development CO., Ltd. The remaining authors declare no competing financial interests.

Author Contributions

R.Z. and A.G. contributed equally to this work. S.W., A.G., and M.W. designed the experiments and supervised the project. R.Z. prepared all the solid electrolytes and conducted the air exposure measurements. S.L. conducted the SEM-EDX measurements. A.G. carried out the NMR measurements and analyzed the results. E.S. conducted the NPD measurements and A.G. analyzed the data. K.C. assembled the solid-state batteries and conducted the cycling test. All authors discussed the results and contributed to the preparation of the manuscript.

Data Availability Statement

The data that support the findings of this study are available from the corresponding author upon reasonable request.

Keywords

air stability, ionic conductivity, lithium argyrodites thioarsenate, solid electrolytes, structure-transport correlations

Received: October 31, 2024
Revised: December 14, 2024
Published online:

[1] J. B. Goodenough, Y. Kim, *Chem. Mater.* **2010**, *22*, 587.
[2] J. B. Goodenough, K. S. Park, *J. Am. Chem. Soc.* **2013**, *135*, 1167.
[3] J. Janek, W. G. Zeier, *Nat. Energy.* **2016**, *1*, 16141.
[4] F. Chu, M. Wang, J. Liu, Z. Guan, H. Yu, B. Liu, F. Wu, *Adv. Funct. Mater.* **2022**, *32*, 202205393.
[5] Z. Guan, X. Chen, F. Chu, R. Deng, S. Wang, J. Liu, F. Wu, *Adv. Energy Mater.* **2023**, *13*, 202302850.
[6] T. Famprikis, P. Canepa, J. A. Dawson, M. S. Islam, C. Masquelier, *Nat. Mater.* **2019**, *18*, 1278.
[7] A. Gautam, M. Ghidiu, E. Suard, M. A. Kraft, W. G. Zeier, *ACS Appl. Energy Mater.* **2021**, *4*, 7309.
[8] A. Gautam, M. Ghidiu, A.-L. Hansen, S. Ohno, W. G. Zeier, *Inorg. Chem.* **2021**, *60*, 18975.
[9] A. Gautam, M. Sadowski, M. Ghidiu, N. Minafra, A. Senyshyn, K. Albe, W. G. Zeier, *Adv. Energy Mater.* **2021**, *11*, 202003369.
[10] B. Helm, R. Schlem, B. Wankmiller, A. Banik, A. Gautam, J. Ruhl, C. Li, M. R. Hansen, W. G. Zeier, *Chem. Mater.* **2021**, *33*, 4773.
[11] A. Gautam, M. Sadowski, N. Prinz, H. Eickhoff, N. Minafra, M. Ghidiu, S. P. Culver, K. Albe, T. F. Fässler, M. Zobel, W. G. Zeier, *Chem. Mater.* **2019**, *31*, 10178.
[12] S. Wang, W. Zhang, X. Chen, D. Das, R. Ruess, A. Gautam, F. Walther, S. Ohno, R. Koerver, Q. Zhang, W. G. Zeier, F. H. Richter, C. W. Nan, J. Janek, *Adv. Energy Mater.* **2021**, *11*, 1.
[13] T. Bernges, S. P. Culver, N. Minafra, R. Koerver, W. G. Zeier, *Inorg. Chem.* **2018**, *57*, 13920.
[14] S. Ohno, B. Helm, T. Fuchs, G. Dewald, M. A. Kraft, S. P. Culver, A. Senyshyn, W. G. Zeier, *Chem. Mater.* **2019**, *31*, 4936.
[15] K. Hogrefe, N. Minafra, I. Hanghofer, A. Banik, W. G. Zeier, H. M. R. Wilkening, *J Am. Chem. Soc.* **2022**, *144*, 1795.
[16] I. Hanghofer, M. Brinek, S. L. Eisbacher, B. Bitschnau, M. Volck, V. Hennige, I. Hanzu, D. Rettenwander, H. M. R. Wilkening, *Phys. Chem. Chem. Phys.* **2019**, *21*, 8489.
[17] V. Epp, Ö. Gün, H. J. Deiseroth, M. Wilkening, *J. Phys. Chem. Lett.* **2013**, *4*, 2118.
[18] H. J. Deiseroth, J. Maier, K. Weichert, V. Nickel, S. T. Kong, C. Reiner, *Z Anorg. Allg. Chem.* **2011**, *637*, 1287.
[19] S. T. Kong, H. J. Deiseroth, J. Maier, V. Nickel, K. Weichert, C. Reiner, *Z Anorg. Allg. Chem.* **2010**, *636*, 1920.
[20] S. T. Kong, Ö. Gün, B. Koch, H. J. Deiseroth, H. Eckert, C. Reiner, *Chem-eur J.* **2010**, *16*, 5138.
[21] H. J. Deiseroth, S. T. Kong, H. Eckert, J. Vannahme, C. Reiner, T. Zaiß, M. Schlosser, *Angew. Chem., Int. Ed.* **2008**, *47*, 755.
[22] A. Morscher, B. B. Duff, G. Han, L. M. Daniels, Y. Dang, M. Zanella, M. Sonni, A. Malik, M. S. Dyer, R. Chen, F. Blanc, J. B. Claridge, M. J. Rosseinsky, *J. Am. Chem. Soc.* **2022**, *144*, 22178.
[23] A. Gautam, H. Al-Kutubi, T. Famprikis, S. Ganapathy, M. Wagemaker, *Chem. Mater.* **2023**, *35*, 8081.
[24] N. J. J. De Klerk, I. Rosłoń, M. Wagemaker, *Chem. Mater.* **2016**, *28*, 7955.
[25] C. Yu, S. Ganapathy, N. J. J. De Klerk, I. Roslon, E. R. H. Van Eck, A. P. M. Kentgens, M. Wagemaker, *J Am. Chem. Soc.* **2016**, *138*, 11192.
[26] N. Masuda, K. Kobayashi, F. Utsuno, T. Uchikoshi, N. Kuwata, *J Phys. Chem. C.* **2022**, *126*, 14067.
[27] T. K. Schwietert, A. Gautam, A. K. Lavrinenko, D. Drost, T. Famprikis, M. Wagemaker, A. Vasileiadis, *Mater. Adv.* **2024**, *5*, 1952.
[28] M. Inagaki, K. Suzuki, S. Hori, K. Yoshino, N. Matsui, M. Yonemura, M. Hirayama, R. Kanno, *Chem. Mater.* **2019**, *31*, 3485.
[29] P. Adeli, J. D. Bazak, K. H. Park, I. Kochetkov, A. Huq, G. R. Goward, L. F. Nazar, *Angew. Chem., Int. Ed.* **2019**, *58*, 8681.
[30] M. V. Reddy, C. M. Julien, A. Mauger, K. Zaghib, *Nanomaterials.* **2020**, *10*, 1606.
[31] D. H. S. Tan, E. A. Wu, H. Nguyen, Z. Chen, M. A. T. Marple, J. M. Doux, X. Wang, H. Yang, A. Banerjee, Y. S. Meng, *ACS Energy Lett.* **2019**, *4*, 2418.
[32] E. Zhao, L. He, Z. Zhang, J.-M. Doux, D. H. S. Tan, E. A. Wu, G. Deysher, Y.-T. Chen, J. Zhao, F. Wang, Y. S. Meng, *Chem. Commun.* **2021**, *57*, 10787.
[33] Y. Wang, X. Lü, C. Zheng, X. Liu, Z. Chen, W. Yang, J. Lin, F. Huang, *Angew. Chem., Int. Ed.* **2019**, *131*, 7755.
[34] F. Zhao, J. Liang, C. Yu, Q. Sun, X. Li, K. Adair, C. Wang, Y. Zhao, S. Zhang, W. Li, S. Deng, R. Li, Y. Huang, H. Huang, L. Zhang, S. Zhao, S. Lu, X. Sun, *Adv. Energy Mater.* **2020**, *10*, 201903422.
[35] G. Sahu, Z. Lin, J. Li, Z. Liu, N. Dudney, C. Liang, *Energy Environ. Sci.* **2014**, *7*, 1053.
[36] J. Liang, N. Chen, X. Li, X. Li, K. R. Adair, J. Li, C. Wang, C. Yu, M. Norouzi Banis, L. Zhang, S. Zhao, S. Lu, H. Huang, R. Li, Y. Huang, X. Sun, *Chem. Mater.* **2020**, *32*, 2664.
[37] P. Lu, Y. Xia, G. Sun, D. Wu, S. Wu, W. Yan, X. Zhu, J. Lu, Q. Niu, S. Shi, Z. Sha, L. Chen, H. Li, F. Wu, *Nat. Commun.* **2023**, *14*, 4077.
[38] J. Lin, M. Schaller, S. Indris, V. Baran, A. Gautam, J. Janek, A. Kondrakov, T. Brezesinski, F. Strauss, *Angew. Chem., Int. Ed.* **2024**, *63*, e202404874.
[39] G. Sahu, E. Rangasamy, J. Li, Y. Chen, K. An, N. Dudney, C. Liang, *J. Mater. Chem. A.* **2014**, *2*, 10396.
[40] A. A. Coelho, *TOPAS-Academic*, Coelho Software, Brisbane, Australia **2007**.
[41] P. Wang, H. Liu, S. Patel, X. Feng, P. H. Chien, Y. Wang, Y. Y. Hu, *Chem. Mater.* **2020**, *32*, 3833.
[42] A. Yelon, B. Movaghar, H. M. Branz, *Phys. Rev. B.* **1992**, *46*, 12244.
[43] M. Brinek, C. Hiebl, H. M. R. Wilkening, *Chem. Mater.* **2020**, *32*, 4754.